Pramana – J. Phys. (2022) 96:8
https://doi.org/10.1007/s12043-021-02251-5

A combined Glauber model plus relativistic Hartree–Bogoliubov theory analysis of nuclear reactions with light and medium mass nuclei

AJEET SINGH[1], A SHUKLA[1,*] and M K GAIDAROV[2]

[1]Department of Physics, Rajiv Gandhi Institute of Petroleum Technology, Jais, Amethi 229 305, India
[2]Institute for Nuclear Research and Nuclear Energy, Bulgarian Academy of Sciences, 1784 Sofla, Bulgaria
*Corresponding author. E-mail: amritanshu.shukla@gmail.com

MS received 29 January 2021; revised 12 August 2021; accepted 18 August 2021

Abstract. In the present work, we have performed systematic studies of nuclear reactions of various light and medium mass nuclei (He, Li, Be, B, C, Ca, Ni, Zr and Sn isotopes) on ^{12}C and proton targets mainly at high energies using Glauber model and a comparison of the results with available experimental data is made. The microscopic nuclear densities needed for these calculations have been obtained using relativistic Hartree–Bogoliubov formalism. In addition, other ground-state bulk properties are also calculated and compared with the available experimental data. It has been observed that the results obtained using the relativistic framework with the density-dependent meson exchange (DD-ME2) parameter set are in better agreement with the experimental data than with the density-dependent point coupling (DD-PC1) results. Also, we have seen that the total reaction cross-section increases with the increase of the projectile mass. The differential elastic scattering cross-section results obtained with both parameter sets are almost identical at low scattering angles and compare well with the experimental data. However, at higher scattering angles, they show significant differences from the experimental data.

Keywords. Binding energy; relativistic Hartree–Bogoliubov formalism; Glauber theory; total nuclear reaction cross-section.

PACS Nos 24; 24.10.-i

1. Introduction

Recently, the radioactive ion beam (RIB) facilities and advanced detection technologies have become standard tools to study nuclear structure and reaction properties of nuclei lying at the drip line (far away from the β stability line). The quantities measured in various nuclear reactions include the total reaction cross-sections, elastic scattering differential cross-sections, nucleon removal cross-sections, nuclear and Coulomb breakup cross-sections and momentum distributions of fragments in breakup processes on nuclear targets. These observables have been used to study the nuclear structure of unstable nuclei in detail, particularly the halo structure near the drip lines [1–4]. From another side it has been found quite useful to understand the role of nuclear interaction, especially at proton/neutron drip line, as these reaction characteristics exhibit many interesting nuclear structural features, such as one/two neutron halo, skin effect, deformations, bubbleness and magicity/emergence of new shell gaps [5,6]. The measurement of the total reaction and differential cross-sections are particularly useful for these unstable nuclei as the effects produced by weekly bound neutron/proton nuclei are quite different from the nuclear core. For stable nuclei, electron and proton elastic scattering data provide the charge and matter density distributions, while for unstable nuclei, not only electron elastic scattering experiments are yet to be performed, but also proton scattering data obtained from RIBs colliding with a proton target [7,8] are scarce. Hence, deduction of the rms matter radius of unstable nuclei is mainly performed through measurements of reaction cross-section only.

The measurement of reaction cross-sections and matter radii of ^{6,8}He, ^{11}Li and ^{11,14}Be [7–9] has shown anomalously large values compared to that of the neighbouring nuclei. Also, very recently, the measured interaction cross-sections of very neutron-rich carbon

Published online: 22 December 2021

isotopes have ^{22}C deduced to be a two-neutron halo nucleus (the ^{21}C nucleus is unstable) [10–12]. The momentum distribution and the one-neutron removal cross-section have also shown that ^{22}C is a halo nucleus and $N = 16$ is considered to be a new magic number in neutron-rich nuclei [13]. The observation of such nuclear halo and other novel features are closely connected with the evolution of the shell structure in He, Li, Be, B and C isotopes. These investigations have stimulated several theoretical studies in the past [14,15], yet it needs further refinement to reduce the theoretical uncertainty and to constrain the theoretical approaches. These are the arguments that motivate us to study the nuclear reaction cross-sections of such nuclei consistently with nuclear structure details. For these calculations, realistic nuclear density is required, which can be obtained from a certain number of nuclear models. Hence, it is very important to choose a suitable set of density/wave functions before employing them for further calculations. We have used the relativistic Hartree–Bogoliubov (RHB) model for calculating the ground-state properties of nuclei considered in the present paper. Cross-section studies have been performed using the Glauber model which can account for the breakup effect of the weakly bound nucleus [16,17]. The Glauber model has been successfully applied to study high-energy nucleus–nucleus reaction cross-section data. The model is based on the eikonal approximation which exhibits complex behaviour compared to nucleon–nucleon interaction [18,19]. The main input to obtain the reaction cross-sections through Glauber model is the structural information of the nuclei involved, which is provided through the density profile. The Glauber model predicts the values of total reaction cross-sections at higher energies which are much closer to the experimental data. In our previous studies, we have shown that the density obtained from the relativistic mean-field can be used effectively for reaction studies [20–22].

In the present work, we have calculated the nuclear reaction properties of even–even $^{4-8}$He,$^{6-10}$Li, $^{10-14}$Be, $^{8-16}$B, $^{10-22}$C, ^{40}Ca, ^{58}Ni, ^{90}Zr and ^{120}Sn nuclei extending from the proton to the neutron drip line. The evaluation of the credibility of the nuclear densities used as inputs for reaction studies has been performed by comparing the nuclear ground-state properties, i.e. the binding energies and charge radii, with the corresponding experimental values. The ground-state properties of the considered nuclei are calculated using the relativistic Hartree–Bogoliubov model with density-dependent meson exchange (DD-ME2) and point coupling (DD-PC1) interactions and with separable pairing interaction. The nuclear reaction cross-section for light nuclei, such as He, Li, Be, B and C isotopes, as the projectiles on the ^{12}C target are calculated using the Glauber model, with densities obtained from RHB formalism. We have also calculated the reaction cross-section in medium mass nuclei, namely Ca, Ni, Zr and Sn isotopes, on proton target. The elastic scattering differential cross-sections are also analysed for various projectile energies. They give different types of diffraction patterns which depend on the diffuseness of the nuclear surface.

The paper is organised in the following manner. In §2 we discuss the theoretical formalism used in the present work. The results for the ground-state properties (binding energies, charge radii, density distributions, reaction cross-sections) are presented in §3, where a comparison with the available experimental data is also given. Finally, the summary of the results and conclusions are presented in §4.

2. Mathematical formalism

2.1 *RHB theory*

The relativistic Hartree–Bogoliubov (RHB) model [22] is based on the density-dependent effective interactions. Density-dependent meson exchange and point coupling interactions are used for the analysis of nuclear structural phenomena. These models are briefly discussed in the following subsections.

2.1.1 *DD-ME2.* The Lagrangian density for DD-ME2 interaction is given by

$$\begin{aligned}\mathcal{L} = \overline{\Psi}[\gamma(\iota\partial - g_\omega\omega - g_\rho\vec{\rho}\vec{\tau} - eA) - m - g_\sigma\sigma]\Psi \\ +\frac{1}{2}(\partial\sigma)^2 - \frac{1}{2}m_\sigma^2\sigma^2 \\ -\frac{1}{4}\Omega_{\mu\nu}\Omega^{\mu\nu} + \frac{1}{2}m_\omega^2\omega^2 - \frac{1}{4}\vec{R}_{\mu\nu}\cdot\vec{R}^{\mu\nu} \\ +\frac{1}{2}m_\rho^2\vec{\rho}_\mu\cdot\vec{\rho}^\mu - \frac{1}{4}F_{\mu\nu}F^{\mu\nu},\end{aligned} \tag{1}$$

where Ψ is the Dirac spinor and m denotes the bare nucleon mass. m_σ, m_ω and m_ρ are the masses of σ, ω and ρ mesons, respectively . g_σ, g_ω and g_ρ and $\frac{e^2}{4\pi} = \frac{1}{137}$ are the coupling constants for the σ, ω and ρ mesons and photons, respectively. $\vec{\tau}$ denotes the Pauli isospin matrices. $\Omega^{\mu\nu}$, $R^{\mu\nu}$ and $F^{\mu\nu}$ as field tensors of the vector field ω, ρ and photon can be written as

$$\Omega^{\mu\nu} = \partial^\mu\omega^\nu - \partial^\nu\omega^\mu, \tag{2}$$

$$\vec{R}^{\mu\nu} = \partial^\mu\vec{\rho}^\nu - \partial^\nu\vec{\rho}\mu, \tag{3}$$

$$F^{\mu\nu} = \partial^\mu A^\nu - \partial^\nu A^\mu. \tag{4}$$

We obtain the total energy by integrating the Hamiltonian density over the r-space which depends on the

Dirac spinors Ψ, $\overline{\Psi}$ and the meson fields σ, ω^μ, $\vec{\rho}^\mu$, A^μ:

$$E_{\mathrm{RMF}}[\Psi, \overline{\Psi}, \sigma, \omega^\mu, \vec{\rho}^\mu, A^\mu] = \int \mathrm{d}^3 r H(r). \tag{5}$$

The coupling of σ-meson and ω-meson to the nucleon field [23–25] in the phenomenological approach is given by

$$g_i(\rho) = g_i(\rho_{\mathrm{sat}}) f_i(x) \quad \text{for} \quad i = \sigma, \omega, \tag{6}$$

where

$$f_i(x) = a_i \frac{1 + b_i(x + d_i)^2}{1 + c_i(x + d_i)^2} \tag{7}$$

is a function of $x = \rho/\rho_{\mathrm{sat}}$ and ρ_{sat} denotes the baryon density at saturation in symmetric nuclear matter. The eight real parameters in (6) are not independent. The five constraints $f_i(1) = 1$, $f''_\sigma(1) = f''_\omega(1)$ and $f''_i(0) = 0$, reduce the number of independent parameters to three. Three additional parameters in the isoscalar channel are $g_\sigma(\rho_{\mathrm{sat}})$, $g_\omega(\rho_{\mathrm{sat}})$ and m_σ, the mass of the phenomenological σ-meson. The asymmetric nuclear matter calculations [26] within the Dirac–Brueckner approach suggested the functional form of the density dependence of ρ-meson couplings as

$$g_\rho(\rho) = g_\rho(\rho_{\mathrm{sat}}) \mathrm{e}^{-a_\rho(x-1)}. \tag{8}$$

The isovector channel is parametrised by $g_\rho(\rho_{\mathrm{sat}})$ and a_ρ. The DD-ME2 parameter set used in the present study is given in table 1.

2.1.2 *DD-PC1.* The effective Lagrangian for the density-dependent point coupling interaction is given by [27]

$$\begin{aligned}\mathcal{L} = {} & \overline{\Psi}(i\gamma \cdot \partial - m)\Psi - \frac{1}{2}\alpha_s(\widehat{\rho})(\overline{\Psi}\Psi)(\overline{\Psi}\Psi) \\ & - \frac{1}{2}\alpha_v(\widehat{\rho})(\overline{\Psi}\gamma^\mu\Psi)(\overline{\Psi}\gamma_\mu\Psi) \\ & - \frac{1}{2}\alpha_{TV}(\rho)(\overline{\Psi}\vec{\tau}\gamma^\mu\Psi)(\overline{\Psi}\vec{\tau}\gamma_\mu\Psi) \\ & + \frac{1}{2}\delta_s(\partial_\nu\overline{\Psi}\Psi)(\partial^\nu\overline{\Psi}\Psi) \\ & - e\overline{\Psi}\gamma \cdot A\frac{(1-\tau_3)}{2}\Psi. \end{aligned} \tag{9}$$

The total energy-density functional of RMF for the point coupling model can be written as

$$E_{\mathrm{RMF}}[\Psi, \overline{\Psi}, A_\mu] = \int \mathrm{d}^3 r H(r), \tag{10}$$

where the Hamiltonian density $H(r)$ can be obtained from the Lagrangian density. The functional form of the couplings is given by

$$\alpha_i(\rho) = a_i + (b_i + c_i x)\mathrm{e}^{-d_i x}, \quad i \equiv S, V, TV, \tag{11}$$

with $x = \rho/\rho_{\mathrm{sat}}$, where ρ_{sat} denotes the nucleon density at saturation in symmetric nuclear matter. The details of the DD-PC1 parameter set are given in table 2.

2.1.3 *RHB theory with a pairing interaction.* The RHB model represents a relativistic extension of the conventional Hartree–Bogoliubov framework in which mean-field and pairing correlations are treated self-consistently [28]. The RHB model gives a unified description of particle–hole (ph) and particle–particle (pp) correlations on a mean-field level by using the average self-consistent mean-field potential that encloses the long-range ph correlations and a pairing field potential which sums up the pp correlations. The density matrix in the presence of pairing is generalised to two densities, the normal density $\widehat{\rho}$ and pairing tensor $\widehat{k}$. The RHB energy-density functional can be written as

$$E_{\mathrm{RHB}}[\widehat{\rho}, \widehat{k}] = E_{\mathrm{RMF}}[\widehat{\rho}] + E_{\mathrm{pair}}[\widehat{k}]. \tag{12}$$

The pairing part of the RHB functional is given by

$$E_{\mathrm{pair}}[\widehat{k}] = \frac{1}{4}\sum_{n_1 n_1'}\sum_{n_2 n_2'} k^*_{n_1 n_1'} \langle n_1 n_1' | V^{PP} | n_2 n_2' \rangle k_{n_2 n_2'}, \tag{13}$$

where $\langle n_1 n_1' | V^{PP} | n_2 n_2' \rangle k_{n_2 n_2'}$ are the matrix elements of the two-body pairing interaction and indices n_1, n_1',n_2 and n_2' denote quantum numbers that specify the Dirac indices of the spinor. The pairing interaction is taken in the form

$$V^{PP}(r_1, r_2, r_1', r_2') = -G\delta(R - R')P(r)P(r'), \tag{14}$$

where

$$R = \frac{1}{\sqrt{2}}(r_1 + r_2)$$

and

$$r = \frac{1}{\sqrt{2}}(r_1 - r_2)$$

represent the centre of mass and the relative coordinates and the form factor $P(r)$ is the Fourier transform of $p(k)$:

$$P(r) = \frac{1}{(4\pi a^2)^{\frac{3}{2}}}\mathrm{e}^{-\frac{r^2}{2a^2}}. \tag{15}$$

The pairing force has a finite range and, because of the factor $\delta(R - R')$, it preserves the translational invariance. Finally, the pairing energy in the nuclear ground state is given by [29]

$$E_{\mathrm{pair}} = -G\sum_N P^*_N P_N. \tag{16}$$

Table 1. The parameter sets of DD-ME2.

$M = 939.00$	$m_\omega = 783.00$	$m_\rho = 763.00$	$m_\sigma = 550.124$
$g_\sigma(\rho_{(\text{sat})}) = 10.5396$	$g_\omega(\rho_{(\text{sat})}) = 13.0189$	$g_\rho(\rho_{(\text{sat})}) = 3.6836$	$a_p = 0.5008$
$a_\sigma = 1.3854$	$a_\omega = 1.3879$	$b_\sigma = 0.9781$	$b_\omega = 0.8525$
$c_\sigma = 1.5342$	$c_\omega = 1.3566$	$d_\sigma = 0.4661$	$d_\omega = 0.4957$

Table 2. The parameter sets of DD-PC1.

$M = 939.00$	$m_\omega = 783.00$	$m_\rho = 763.00$	$m_\sigma = 550.124$
$a_S\,(\text{fm}^2) = -10.0462$	$b_S\,(\text{fm}^2) = -9.1504$	$c_S\,(\text{fm}^2) = -6.4273$	$d_S = 1.3724$
$a_V\,(\text{fm}^2) = 5.9195$	$b_V\,(\text{fm}^2) = 8.8637$	$d_V = 0.6584$	$b_{TV}\,(\text{fm}^2) = 1.8360$
$d_{TV} = 0.6403$	$\delta_S\,(\text{fm}^4) = -0.8149$		

2.2 *Reaction cross-section using the Glauber model*

2.2.1 *Total reaction cross-section.* The well-known Glauber model has been established to reproduce the experimental data at high energies. However, it fails to describe reasonably the collisions induced at relatively low energies. In such a case, the Glauber model is modified to take care of finite range effects in the profile function and Coulomb-modified trajectories. The details to calculate the reaction cross-sections using the Glauber approach has been given by Glauber [30]. The standard Glauber form for the total reaction cross-section at high energies is expressed [31–33] as

$$\sigma_R = 2\pi \int_0^\infty b[1 - T(b)]\mathrm{d}b, \tag{17}$$

where $T(b)$ is the transparency function at impact parameter b. The function $T(b)$ is calculated in the overlap region between the projectile and the target, assuming that the interaction is formed from a single nucleon–nucleon (NN) collision. It is given by [3]

$$T(b) = \exp\left[-\sum_{i,j}\overline{\sigma}_{i,j}\int \mathrm{d}\vec{s}\,\overline{\rho}_{ti}(s)\overline{\rho}_{pj}(|\vec{b}-\vec{s}|s)\right]. \tag{18}$$

Here the summation is over the nucleons i and j, where i belongs to the projectile and j belongs to the target nuclei. The subscripts p and t refer to the projectile and the target, respectively. $\overline{\sigma}_{i,j}$ is the experimental nucleon–nucleon reaction cross-section which depends on the energy. The argument of $T(b)$ in eq. (18) is $(|\vec{b} - \vec{s}|)$, which stands for the impact parameter between the ith and the jth nucleons. The Glauber model is designed for high-energy approximation. However, it was found to work fairly well, for both the nucleus–nucleus reaction cross-sections and the differential elastic scattering cross-sections, over a broad energy range [34,35]. Thus, for the finite range approximation, the transparency function is given by [36,37]

$$T(b) = \exp\left[-\int_{P,T}\sum_{i,j}[\Gamma_{ij}(\vec{b}-\vec{s}+\vec{t})]\overline{\rho}_{Pi}(\vec{t})\overline{\rho}_{Tj}(\vec{s})\mathrm{d}\vec{s}\mathrm{d}\vec{t}\right], \tag{19}$$

where the summation indices i and j run over neutron and proton for both the target and the projectile. Here the profile function Γ_{NN} for optical limit approximation is defined as

$$\Gamma_{NN} = \Gamma_{ij}(b_{\text{eff}}) = \frac{1 - i\alpha_{NN}}{2\pi\beta_{NN}^2}\sigma_{NN}\exp\left(-\frac{b_{\text{eff}}^2}{2\beta_{NN}^2}\right) \tag{20}$$

for the finite range and

$$\Gamma_{NN} = \Gamma_{ij}(b_{\text{eff}}) = \frac{1 - i\alpha_{NN}}{2}\sigma_{NN}\delta(b) \tag{21}$$

for the zero range with $b_{\text{eff}} = |\vec{b}-\vec{s}+\vec{t}|$, $\vec{b}$ is the impact parameter in which $\vec{s}$ and $\vec{t}$ are the dummy variables for integration over the z-integrated target and projectile densities.

The model-independent sum-of-Gaussians (SOG) method for analysing nuclear reaction cross-section was originally introduced by Sick [38] and since then it has been applied successfully in numerous studies for deducing nuclear charge/matter distributions from reaction data and also in the Glauber model calculations. Hence $\rho(r)$ can be written as

$$\rho(r) = \sum_{i=1}^{N} c_i \exp[-(r - R_i)^2/\gamma^2], \tag{22}$$

where c_i is the relative width of the ith Gaussian, R_i is the position of the ith Gaussian and γ is the width

of all Gaussian, which is taken as around 1.35 fm [39]. Following the same approach in this work, the nuclear densities obtained from the RHB calculations are fitted to a sum of Gaussian functions. The expression given by (22) is further rearranged to match with the formalism presented in [17] as follows and to extract the needed coefficients c_i and ranges a_i for reaction cross-section calculations.

$$\rho(r) = \sum_{i=1}^{N} c_i \exp[-a_i r^2], \tag{23}$$

where $a_i = (1 - R_i/r)^2/\gamma^2$. Here, the density $\rho(r)$ is normalised to the mass number of nucleons $\int \mathrm{d}r\rho(r) = A$. The nuclear densities written in the Gaussian expansion enable one to calculate reaction cross-section analytically [17]. The parameters σ_{NN}, α_{NN} and β_{NN} depend upon the proton–proton, neutron–neutron and proton–neutron interactions [40]. Then, the Glauber model is used to calculate the total reaction cross-section for both the stable and unstable nuclei considered in the present study.

2.2.2 *Elastic scattering differential cross-section.* One of the advantages of the Glauber theory is that the same input which is used in the reaction cross-section calculation is readily applicable for the calculation of the differential cross-section of elastic scattering. The diffraction pattern in the differential cross-section is expected to depend mainly on the diffuseness of the nuclear surface. Brief details of the mathematical formalism for calculating differential scattering cross-section are presented here. The nucleus–nucleus elastic scattering amplitude is written as

$$F(q) = \frac{iK}{2\pi} \int \mathrm{d}b \mathrm{e}^{iq\cdot b}(1 - \mathrm{e}^{i\chi(b)}). \tag{24}$$

At low energies, this model is modified to include finite range effects in the profile function and Coulomb-modified trajectories. $F(q)$ and $F_{\mathrm{coul}}(q)$ are the elastic and Coulomb (elastic) scattering amplitudes, respectively. The elastic scattering amplitude $F(q)$ is written as

$$F(q) = \mathrm{e}^{i\chi_s}\left\{F_{\mathrm{coul}}(q) + \frac{iK}{2\pi}\int \mathrm{d}b \mathrm{e}^{-iq\cdot b + 2i\eta\ln(Kb)} T(b)\right\} \tag{25}$$

with the Coulomb elastic scattering amplitude $F_{\mathrm{coul}}(q)$ given as

$$F_{\mathrm{coul}}(q) = \frac{-2\eta K}{q^2}\exp\left[-2i\eta\ln\left(\frac{q}{2K}\right) + 2i\arg\Gamma(1+i\eta)\right], \tag{26}$$

where K is the momentum of the projectile and q is the momentum transferred from the projectile to the target. Here $\eta = Z_p Z_t e^2/\hbar v$ is the Sommerfeld parameter, v is the incident velocity and $\chi_s = -2\eta\ln(2Ka)$ with a being the screening radius. The elastic scattering differential cross-section does not depend on the screening radius a [31,41]. The results for the elastic scattering differential cross-sections will be shown in the figures as ratios to the Rutherford cross-sections:

$$\frac{\mathrm{d}\sigma}{\mathrm{d}\sigma_r} = \frac{(\mathrm{d}\sigma/\mathrm{d}\Omega)}{(\mathrm{d}\sigma/\mathrm{d}\Omega)_r} = \frac{|F(q)|^2}{|F_{\mathrm{coul}}(q)|^2}. \tag{27}$$

2.3 *Reaction cross-section using empirical formula*

A large number of empirical formulae (models) with different parameters for total reaction cross-section calculations have been introduced by several researchers [42–54]. These models are developed considering the black sphere model with different modifications added time to time to reproduce the experimental data. The available empirical formula has been compiled in table 3. In the present work, we have also calculated the total reaction cross-section using the empirical formula given by Sihver *et al* [46,48,52] which is discussed below. The model is dependent of the interaction radius R and Coulomb barrier B using strong absorption model [52]:

$$\sigma_R = \pi R^2\left[1 - \frac{B}{E_{\mathrm{cm}}}\right], \tag{28}$$

where R is the interaction radius, E_{cm} is the centre-of-mass energy of the collision and B is the Coulomb barrier of the projectile–target system:

$$B_{\mathrm{Shen}} = \frac{1.44 Z_P Z_T e^2}{R_P + R_T + 3.2} - \frac{R_P R_T}{R_P + R_T},$$
$$R_i = 1.12A_i^{\frac{1}{3}} - 0.94A_i^{-\frac{1}{3}}, \quad i = P, T, \tag{29}$$

where Z_P, Z_T, A_P, A_T, R_P and R_T are the atomic numbers, mass numbers and interaction radius of the projectile (P) and the target (T), respectively. The interaction radius R is given by

$$R_{\mathrm{Shen}} = 1.1\left(A_P^{\frac{1}{3}} + A_T^{\frac{1}{3}} + 1.85\frac{A_P^{\frac{1}{3}}A_T^{\frac{1}{3}}}{A_P^{\frac{1}{3}} + A_T^{\frac{1}{3}}} - C(E)\right) + \frac{5(A_T - 2Z_T)Z_P}{A_P A_T} + 0.176E_{\mathrm{cm}}^{-\frac{1}{3}}\frac{A_P^{\frac{1}{3}}A_T^{\frac{1}{3}}}{A_P^{\frac{1}{3}} + A_T^{\frac{1}{3}}}. \tag{30}$$

The energy-dependent transparency coefficient $C(E)$ is

$$C(E) = 1.91 - 16.0\mathrm{e}^{-0.7274E^{0.3493}} \cos(0.0849E^{0.5904}), \quad (31)$$

where the projectile kinetic energy E is in MeV/nucleon. The calculated reaction cross-section using Shen formula shows good agreement with the experimental data in high-energy region.

For proton as the target, we have calculated the total reaction cross-section using empirical formula given by Wellisch and Axen [54] in terms of mass number of the target A and b_0 is the overlap or transparency parameter (see, for details, ref. [54]):

$$\sigma_R^0 = f_{\mathrm{corr}}\pi r_0^2 \ln N[1 + A^{1/3} - b_0(1 - A^{-1/3})], \quad (32)$$

$$b_0 = 2.247 - 0.915(1 + A^{-1/3}) \quad \text{and} \quad r_0 = 1.36\,\mathrm{fm}, \quad (33)$$

where N is the number of neutrons in the target.

$$f_{\mathrm{corr}} = \frac{1 + 0.15\mathrm{e}^{-E_{\mathrm{kin}}}}{1 + 0.0007A}, \quad (34)$$

$$\sigma_R(\mathrm{Axen}) = f_1(\log_{10} E_{\mathrm{kin}}, A) \cdot f_2(\log_{10} E_{\mathrm{kin}}, A) \cdot \sigma_R^0. \quad (35)$$

The two functions can be written as

$$f_1(x, y) = \frac{1}{1 + \mathrm{e}^{-P_1(y)(x + P_2(y))}} \quad (36)$$

and

$$f_2(x, y) = 1 + P_3(y)\left(1 - \frac{1}{1 + \mathrm{e}^{-P_4(y)(x + P_5(y))}}\right), \quad (37)$$

where x is the $\log_{10} E_{\mathrm{kin}}$ in units of MeV and y is the target atomic number.

$$P_1(y) = \left(8 - \frac{8}{y} - 0.008y\right), \quad (38)$$

$$P_2(y) = 18.72 - \frac{42.2}{y} - 0.0224y, \quad (39)$$

$$P_3(y) = 0.8 + \frac{18}{y} - 0.002y, \quad (40)$$

$$P_4(y) = 5.6 - 0.01y, \quad (41)$$

$$P_5(y) = 10.96\left(1 + \frac{1}{y}\right). \quad (42)$$

3. Results and discussion

This section presents our calculated results of binding energies, charge radius (r_{ch}) and nuclear density for isotopes of He, Li, Be, B, C, Ca, Ni, Zr and Sn using the relativistic Hartree–Bogoliubov theoretical model with DD-ME2 (meson-exchange coupling) and DD-PC1 (point coupling) parameter sets. The calculated results are compared with experimental data.

3.1 *Binding energies, nuclear radii and density profiles*

The calculated binding energies for the considered nuclei along with the experimental values taken from ref. [55] are presented in table 4. It can be seen from table 4 that the calculated binding energies from the RHB formalism are in good agreement with the available experimental data [55,56]. In comparison, the DD-PC1 values of the binding energies are slightly higher than the DD-ME2 values and overestimate the experimental data. For the results given in table 4, the square weighted mean square error with respect to the experimental data is 0.0010 and 0.0011 for DD-ME2 and DD-PC1 parameter sets, respectively. The binding energy of a nucleus indicates the nuclear stability, as well as protons and neutrons decay energies. These results give the confidence to use DD-ME2 and DD-PC1 densities in the calculation of reaction dynamics.

The charge radius (r_{ch}) is obtained from the point proton rms radius through the relation given below [57]:

$$r_c = \sqrt{r_p^2 + 0.64}\,, \quad (43)$$

where the proton radius is considered to be 0.8 fm. In table 4, we have presented the calculated values of charge radius using RHB (DD-ME2 and DD-PC1) formalism along with the experimental data, wherever available [58]. It is found that the calculated values of the charge radius agree well with the experimental ones. For instance, the obtained values of r_{ch} for ^{12}C with DD-ME2 and DD-PC1 are 2.507 and 2.552 fm, respectively and they compare well with the measured value of 2.47 fm. As can be seen, the calculated values of charge radii are slightly higher for DD-PC1 than for the DD-ME2 parameter set. For the results given in table 4, the square weighted mean square errors with respect to the experimental data are 0.0036 and 0.0043 for DD-ME2 and DD-PC1 parameter sets, respectively. Since the charge radius is obtained from the density profile, our RHB results for charge radii match well with the experimental results. We have used these densities to find coefficients c_i and ranges a_i for reaction cross-section calculations.

To check the reliability of the calculated total nuclear densities, we have compared the calculated charge densities with the available experimental data (for ^{40}Ca and ^{90}Zr), as shown in figure 1. Figure 1 represents the densities of ^{40}Ca and ^{90}Zr as a function of radial distance r. In figure 1a, the nuclear charge densities with and without

Table 3. List of empirical formulae for reaction cross-section calculations.

Interaction	Models	Relation/Value	Reference
Nucleus–Nucleus	Bradt–Peters	$\sigma_R = \pi r_0^2 (A_P^{\frac{1}{3}} + A_T^{\frac{1}{3}} - \delta)^2$	[42]
	Kox	$\sigma_R = \pi r_0^2 (A_P^{\frac{1}{3}} + A_T^{\frac{1}{3}} - \delta)^2 (1 - \frac{B_C}{E_{\rm cm}})$	[43]
	Kox	$\sigma_R = \pi r_0^2 (A_P^{\frac{1}{3}} + A_T^{\frac{1}{3}} - a\frac{A_P^{\frac{1}{3}} A_T^{\frac{1}{3}}}{A_P^{\frac{1}{3}} + A_T^{\frac{1}{3}}} - C)^2 (1 - \frac{B_C}{E_{\rm cm}})$	[44]
	Kox	$\sigma_R = \pi R_{\rm int}^2 (1 - \frac{B_C}{E_{\rm cm}})$	[45,46]
	Townsend	$\sigma_R = \pi R_{\rm int}^2 (1 - \frac{B_c}{E_{\rm cm}})$, $R_{\rm int} = R_{\rm vol} + R_{\rm surf}$	[47]
	Shen	$\sigma_R = 10\pi R_{\rm int}^2 (1 - \frac{B}{E_{\rm cm}})$	[46,48]
	Sihver	$\sigma_R = \pi r_0^2 [A_P^{\frac{1}{3}} + A_T^{\frac{1}{3}} - b_0 [A_P^{\frac{-1}{3}} + A^{\frac{-1}{3}}]]^2$	[46,49]
	Tripathi	$\sigma_R = \pi r_0^2 (A_P^{\frac{1}{3}} + A_T^{\frac{1}{3}} + \delta_E)^2 (1 - R_c \frac{B}{E_{\rm cm}}) X_m$	[46,50]
	Kei Iida	$\sigma_R = \pi [(a_{P0} + \Delta ap) f_p^{\frac{1}{2}} + (a_{T0} + \Delta a_T) f_T^{\frac{1}{2}}]^2$	[51]
	Sihver	$\sigma_R = \pi R^2 (1 - \frac{B}{E_{\rm cm}})$	[46,52]
Proton–Nucleus	Sihver	$\sigma_R = \pi r_0^2 [1 + A_T^{\frac{1}{3}} - b_0 [1 + A^{\frac{-1}{3}}]]^2$	[49]
	Tripathi	$\sigma_R = \pi r_0^2 (A_P^{\frac{1}{3}} + A_T^{\frac{1}{3}} + \delta_E)^2 (1 - \frac{B}{E_{\rm cm}})$	[53]
	Axen	$\sigma_R = f_1(\log_{10} E_{\rm kin}, A) \cdot f_2(\log_{10} E_{\rm kin}, A) \cdot \sigma_R^0)$	[54]
	Kei Iida	$\sigma_R = \pi a_0^2 [1 + (\frac{\rho_0 a_0}{D n_{c0}} - \frac{a_0}{L_0} \frac{{\rm d}L}{{\rm d}a}\vert_0)^{-1} \frac{\Delta\bar{\sigma}_{pN}}{\bar{\sigma}_{pN0}}]^2$	[51]

Table 4. The calculated values of binding energy (in MeV) and charge radius $r_{\rm ch}$ (in fm) for the projectile and target nuclei using RHB (DD-ME2 and DD-PC1) formalism and comparison with experimental data [55,56].

Nucleus	Binding energy			Charge radius $r_{\rm ch}$		
	DD-ME2	DD-PC1	Expt.	DD-ME2	DD-PC1	Expt.
^{4}He	27.818	26.902	28.292	2.140	2.177	1.676
^{6}He	28.979	29.321	29.270	2.118	2.131	2.068
^{8}He	29.626	31.514	31.41	2.124	2.126	1.929
^{6}Li	32.470	32.385	31.994	2.431	2.408	2.539
^{8}Li	42.155	43.042	41.277	2.336	2.331	2.29
^{10}Li	47.669	49.765	45.316	2.342	2.337	–
^{10}Be	61.444	62.191	64.970	2.394	2.420	2.36
^{12}Be	68.916	71.096	68.649	2.461	2.461	–
^{14}Be	66.628	68.185	69.916	2.489	2.488	–
^{8}B	37.865	38.744	37.737	2.725	2.666	–
^{10}B	63.382	64.039	64.751	2.523	2.532	2.428
^{12}B	81.517	82.641	79.575	2.496	2.516	–
^{14}B	87.826	89.425	85.423	2.535	2.545	–
^{16}B	88.076	90.012	88.144	2.566	2.569	–
^{10}C	55.923	56.860	60.321	2.669	2.661	–
^{12}C	87.317	87.517	92.160	2.507	2.552	2.47
^{14}C	104.921	105.766	105.280	2.556	2.585	2.56
^{16}C	108.544	109.970	110.752	2.585	2.607	–
^{18}C	111.792	113.945	115.280	2.612	2.628	–
^{20}C	114.573	117.580	119.18	2.636	2.649	–
^{22}C	116.652	120.562	120.736	2.653	2.663	–
^{40}Ca	342.778	344.791	342.120	3.475	3.457	3.476
^{58}Ni	501.634	501.916	506.459	3.752	3.775	3.774
^{90}Zr	783.195	785.273	783.898	4.268	4.267	4.272
^{120}Sn	1019.399	1020.894	1020.539	4.645	4.645	4.652

Gaussian fitting are illustrated. It is clear from figure 1a that the densities calculated with DD-ME2 and DD-PC1 compare well with the experimental data [59,60] and are almost similar except for a small difference at the centre. In the nucleus, the nucleon density distribution in the central region reaches a maximum and starts decreasing towards the surface. Similarly, we have calculated the densities for ^{90}Zr using DD-ME2 and DD-PC1 parameters and plotted in figure 1b. In the case of ^{40}Ca, the densities obtained using both DDPC1 and DDME2 overestimate slightly the experimental density at the centre, whereas in the case of ^{90}Zr, the results show almost one to one match with the experimental charge density. We have observed that RHB nuclear densities and nuclear densities fitted by a sum of Gaussian functions are quite similar. However, to calculate nuclear reaction cross-section, we require a sum of Gaussian for the total nuclear densities, and hence the coefficient for the same (a_i, c_i) are given in table 5 for both DD-ME2 and DD-PC1 parameter sets.

3.2 *Total reaction cross-section*

One of the main inputs for calculating the reaction cross-section from the Glauber model is the densities of the projectile and the target. We calculate the total nuclear reaction cross-sections for even–even light mass nuclei (as a projectile) on ^{12}C target using the well-known Glauber model for incident energy 30–1100 MeV/nucleon and compared with the experimental data [1,61–63]. To calculate the total reaction cross-section for unstable nuclei, some phenomenological parameters are required to estimate the *NN* cross-section. Here $\overline{\sigma}_{NN}$ is the total reaction cross-section of nucleon–nucleon collisions, α_{NN} is the ratio of the real to the imaginary part of the forward *NN* scattering amplitude and β_{NN} is the slope parameter. The slope parameter determines the fall of the angular distribution of the nucleon–nucleon scattering. These parameters are usually dependent upon the proton–proton, neutron–neutron and proton–neutron interactions. The nucleon–nucleon cross-section ($\overline{\sigma}_{NN}$) is estimated by the expression [64–66]

$$\overline{\sigma}_{NN} = \frac{N_P N_T \sigma_{nn} + Z_P Z_T \sigma_{PP} + N_P Z_T \sigma_{np} + N_T Z_P \sigma_{np}}{A_P A_T}, \tag{44}$$

where A_P, A_T, Z_P, Z_T, N_P, N_T are the mass number, charge number and neutron number of the projectile and the target, respectively .The value of the range parameter β_{NN} as a function of projectile energy E is given by [67,68]

$$\beta_{NN} = 0.99 \exp\left[\frac{-E}{106.679}\right] + 0.089. \tag{45}$$

Figure 2 shows the variation of the total reaction cross-section for ^{12}C projectile on ^{12}C target with experimental data [17,62,63]. It can be seen from figure 2 that the DD-ME2 results match well for all E, particularly at higher values. At low energies, the Coulomb effect breaks the characteristic Glauber assumption that the projectile moves in a straight path along the collision direction, and gives the nucleus–nucleus interaction. The theoretically calculated total reaction cross-section using the Shen formula is also given in figure 2 for comparison. At high projectile energy σ_r is almost constant but in low energy region σ_r decreases with energy. The results obtained with DD-ME2 and DD-PC1 densities are in good agreement with the experimental data. Also, we have presented the values of reaction cross-section obtained from the RMF approach using non-linear terms (NL3) parametrisation [41] in figure 2. As one can see in this figure, the results of the reaction cross-section with RHB (DD-ME2) densities appear slightly better than the ones obtained with RMF (NL3) model.

In figure 3, we present the total reaction cross-sections for $^{4-8}$He, $^{6-10}$Li, $^{10-14}$Be and $^{8-16}$B nuclei on ^{12}C performing calculations with DD-ME2 and DD-PC1 at fixed E = 790 MeV/nucleon and make a comparison with the experimental data [17,62,63]. In addition, we also calculate the total reaction cross-section using the Shen formula. A similar trend is observed for all calculations on different projectiles. Also, the total reaction cross-sections obtained from the DD-ME2 densities agree well with the experimental data.

Figure 4 shows the variation of total reaction cross-section for ^{10,14,16,18,20,22}C on ^{12}C target as a function of the projectile energy in the energy range of 30–1100 MeV/nucleon and experimental results are also given for comparison [17,62,63,69]. The total reaction cross-section is higher at lower incident E (30–200 MeV/nucleon) and start decreasing with the increase of E (400 MeV/nucleon). A small increment in σ_r appears at about 500–800 MeV/nucleon and after that it is constant. The calculated results using the Shen formula at high energy are also constant. We have seen that the total reaction cross-section σ_r also increases with the increase of the projectile mass. For example, the total reaction cross-section for ^{16}C is higher than σ_r for ^{14}C with fixed ^{12}C target. This increase in σ_r may be related to the geometrical area πR^2. The sharp decrease in σ_r with increasing projectile energy up to 400 MeV/nucleon at which point π production causes the total cross-section to rise [70]. This remarkable dip in total reaction cross-section can be attributed to the behaviour of the scattering phase shift.

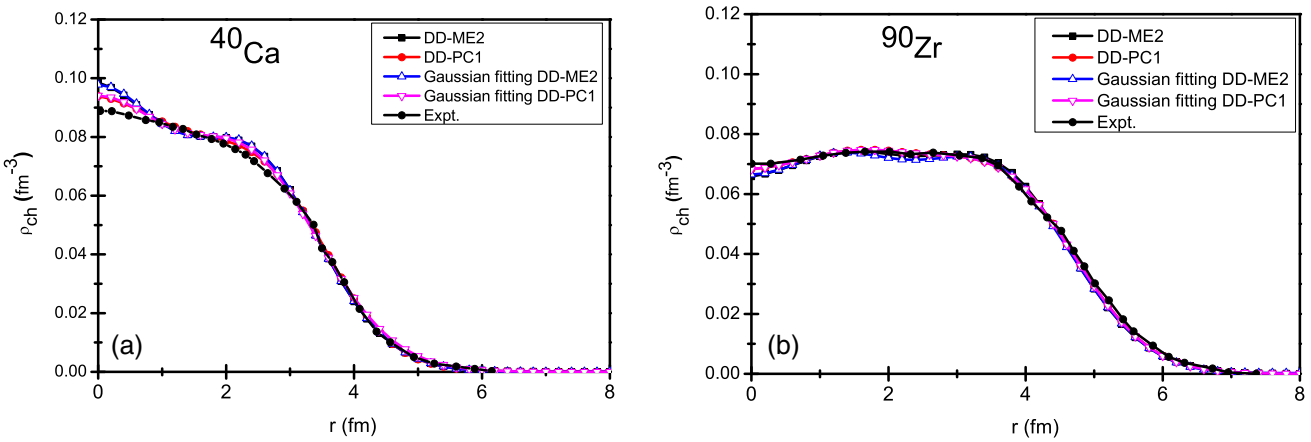

Figure 1. Comparison of charge densities ρ_{ch} obtained from RHB (DD-ME2 and DD-PC1) calculations for ^{40}Ca (**a**) and ^{90}Zr (**b**). Experimental data [59,60] are also given for comparison.

Table 5. The Gaussian coefficients c_1, c_2 (in fm^{-3}) and ranges a_1, a_2 (in fm^{-2}) for the projectile and the target nuclei using RHB (DD-ME2 and DD-PC1) densities.

Nucleus	DD-ME2				DD-PC1			
	c_1	a_1	c_2	a_2	c_1	a_1	c_2	a_2
^{4}He	−1.21074	0.430376	1.40447	0.430362	−1.18094	0.518707	1.33754	0.493431
^{6}He	−1.21274	0.338221	1.40269	0.338139	−1.22195	0.406079	1.38382	0.387125
^{8}He	−1.21473	0.277103	1.40067	0.277053	−0.0344762	0.668599	0.198228	0.266596
^{6}Li	−1.21111	0.331916	1.40443	0.331834	−1.22467	0.418282	1.38844	0.3959
^{8}Li	−0.954186	0.317045	1.15509	0.216906	−1.22505	0.382127	1.39652	0.355307
^{10}Li	−0.0280104	0.746477	0.215441	0.24405	−1.22875	0.345937	1.39616	0.317875
^{10}Be	−0.715954	0.399514	0.932236	0.35115	−2.55755	0.364366	2.74063	0.346752
^{12}Be	−0.144797	0.524765	0.322591	0.255807	−2.95383	0.32823	3.12016	0.312574
^{14}Be	−0.029346	0.884583	0.225294	0.206446	−0.34928	0.338282	0.518984	0.248758
^{8}B	−0.90949	0.280753	1.10632	0.278896	−1.22359	0.377247	1.39324	0.351645
^{10}B	−0.115597	0.560674	0.328971	0.295178	−2.7156	0.365758	2.89883	0.348638
^{12}B	−0.238443	0.500846	0.436427	0.289529	−1.42745	0.353198	1.60728	0.317607
^{14}B	−0.155061	0.53503	0.342766	0.243962	−1.45564	0.322088	1.62735	0.289066
^{16}B	−0.0727572	0.625991	0.267665	0.203858	−2.74612	0.282948	2.91882	0.267825
^{10}C	−0.0714023	0.630206	0.282435	0.279806	−2.42795	0.360827	2.60865	0.342949
^{12}C	−0.252934	0.559829	0.477824	0.312322	−3.57555	0.358487	3.7741	0.342315
^{14}C	−1.11983	0.397884	1.30388	0.328356	−1.78721	0.339177	1.96548	0.306
^{16}C	−0.220029	0.494813	0.40971	0.242021	−4.06649	0.29889	4.24279	0.28573
^{18}C	−0.148886	0.502663	0.342854	0.210082	−1.65748	0.282132	1.83413	0.254483
^{20}C	−0.128874	0.470349	0.324278	0.191071	−1.59376	0.259582	1.7731	0.234468
^{22}C	−0.145042	0.407697	0.340242	0.182128	−1.45633	0.240223	1.64281	0.216755
^{40}Ca	−2.20954	0.182730	2.50586	0.168420	−2.19931	0.172717	2.4568	0.159720
^{58}Ni	−3.01691	0.15353	3.26215	0.1424370	−2.98792	0.149701	3.19114	0.138475
^{90}Zr	−3.39482	0.131204	3.50470	0.121798	−3.30983	0.123187	3.41661	0.114503
^{120}Sn	−3.50362	0.115378	3.67986	0.1044921	−3.49871	0.110147	3.57124	0.099754

The total reaction cross-section for an unstable+unstable projectile–target system is one of the main challenges in experimental nuclear physics. Such measurements give a better understanding of some of the cosmological phenomena such as supernovae, X-ray bursts and in the r-process nucleosynthesis. In recent years, considerable efforts are under way at various laboratories to look for RIB+RIB cross-sections. To study

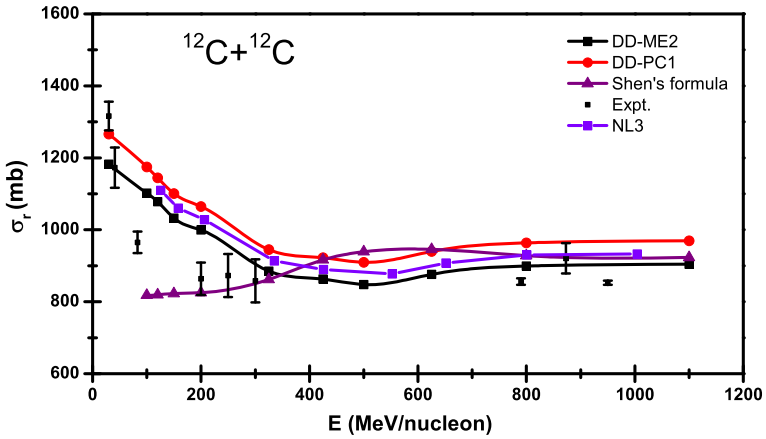

Figure 2. The total nuclear reaction cross-sections σ_r for $^{12}C+^{12}C$ system at different incident energies. The results obtained from DD-ME2, DD-PC1 densities, RMF (NL3) value [41] and Shen formula are compared with the available experimental data [62,63].

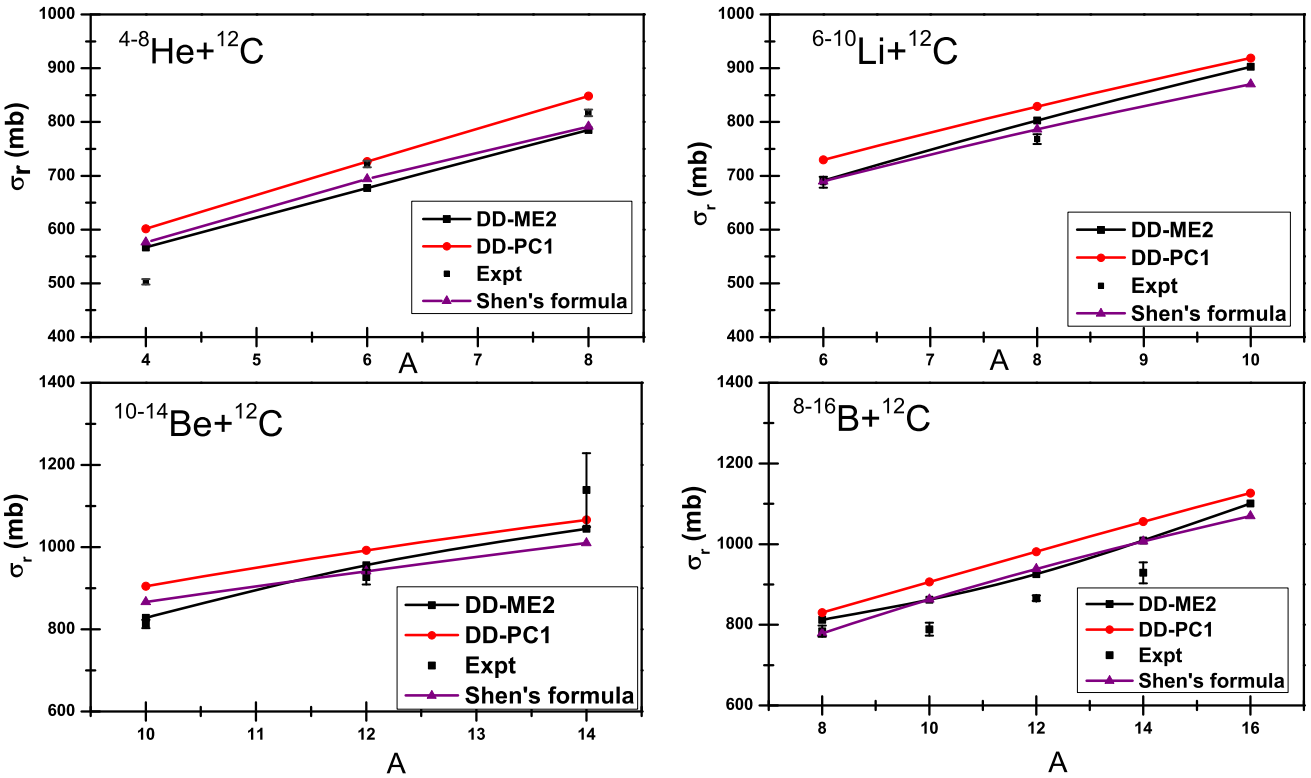

Figure 3. The comparison of total reaction cross-sections at 790 MeV/nucleon for various projectiles (He, Li, Be and B isotopes) on ^{12}C target. Experimental data [17,62,63] are also given for comparison.

the total reaction cross-section for the RIB+RIB system, we select $^{8}Li+^{8}Li$, $^{14}Be+^{14}Be$ and $^{8}B+^{8}B$ systems and the results are presented in figure 5. In the figure, the variation of total reaction cross-section using the densities from DD-ME2 and DD-PC1 parameter sets with various incident energies is shown. We found that the value of σ_r with DD-ME2 is a little bit higher than with the DD-PC1.

The total reaction cross-sections for medium mass nuclei of ^{40}Ca, ^{58}Ni, ^{90}Zr and ^{120}Sn as projectiles on proton target are shown in figure 6. The experimental data are also given for comparison [71]. It is clear from figure 6 that the calculated value of total reaction cross-section is higher at small incident energy and starts decreasing up to 400 MeV/nucleon. σ_r increases in the range of 800 MeV/nucleon and after that, it

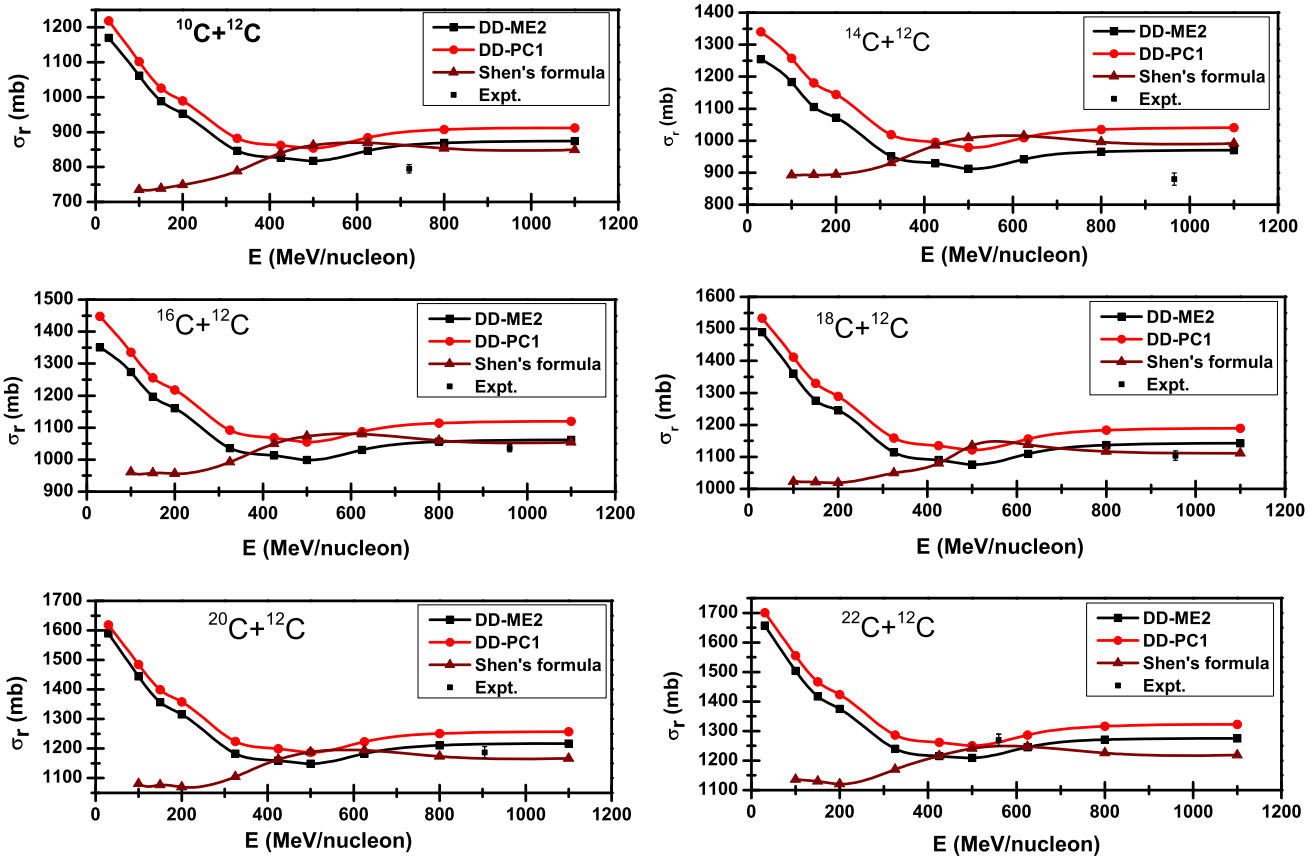

Figure 4. Energy dependence of the total nuclear reaction cross-sections σ_r for ^{10,14,16,18,20,22}C as projectiles on ^{12}C target. The results obtained from DD-ME2 and DD-PC1 densities and Shen formula are compared with the available experimental data [5,62,63].

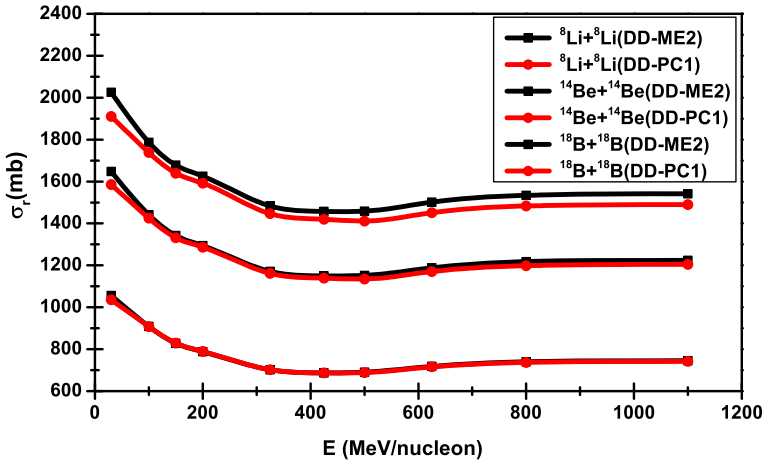

Figure 5. Total reaction cross-sections for ^{8}Li+^{8}Li, ^{14}Be+^{14}Be and ^{18}B+^{18}B systems using RHB densities with different energies.

remains constant. We also calculate the total reaction cross-section using the Axen formula and compare it with the experimental data [71–73]. A similar trend is observed for all calculations on different projectiles. The total reaction cross-sections obtained from the DD-PC1 densities are slightly higher than the ones obtained from

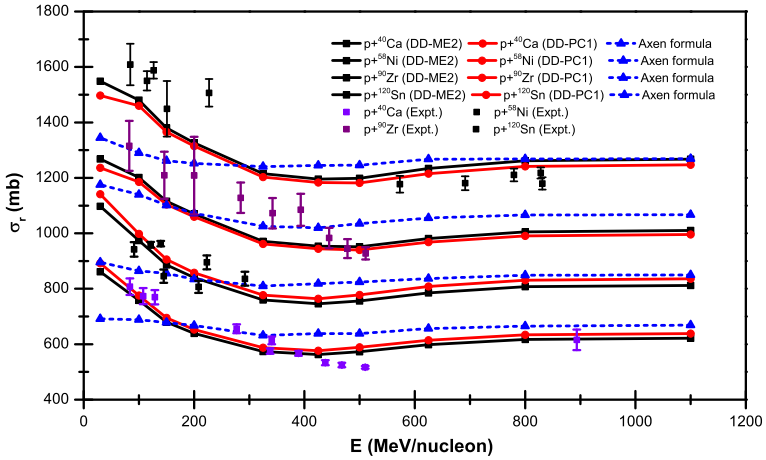

Figure 6. Comparison of total reaction cross-sections at different incident energies for ^{40}Ca, ^{58}Ni, ^{90}Zr and ^{120}Sn as projectiles on proton target. Experimental data [71–73] are also given for comparison.

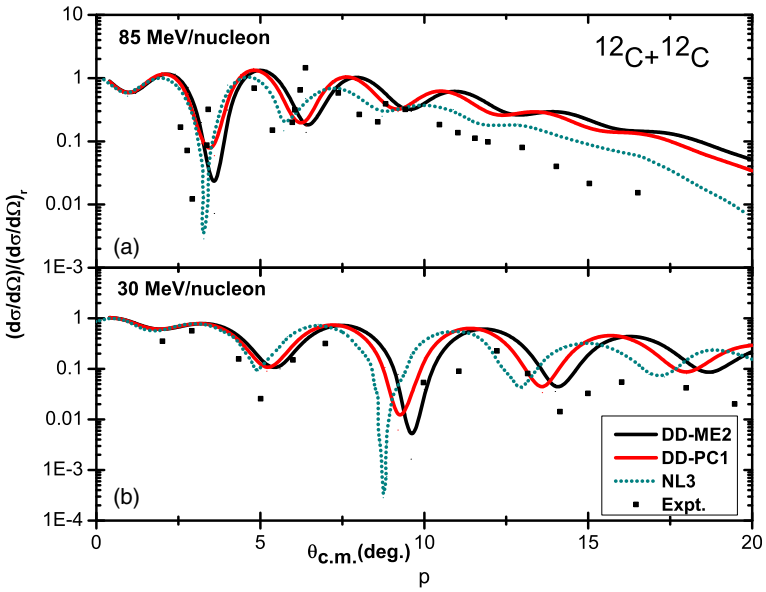

Figure 7. Comparison of elastic scattering differential cross-sections for ^{12}C+^{12}C system at 30 and 85 MeV/nucleon energies with experimental data. The experimental data are taken from [41,61].

the DD-ME2 densities. Also, the total reaction cross-section obtained from the DD-ME2 density agrees well with the experimental values. In low-energy regions, the experimental cross-section overestimates the theoretically obtained cross-sections.

3.3 *Differential elastic scattering cross-section*

We present numerical results for the elastic scattering differential cross-sections [eq. (27)] and compare them with the available experimental results to study how precisely our estimates for the nuclear size lie within the Glauber theory. We start with the calculation of the differential cross-section for ^{12}C+^{12}C system at 30 and 85 MeV/nucleon incident energies as presented in figure 7. The comparison between our theoretical calculations and experimental data shows that the calculated values agree well with the experimental data [41,61], which suggests that the parameters of the *NN* scattering amplitude are well determined. At low angle region, both differential scattering cross-sections (DD-ME2 and DD-PC1) are similar to each other and show oscillatory structure, while at higher angle region, the cross-sections deviate slightly from the experimental data, but the nature of the curve is similar. In general, the results obtained from DD-ME2 and DD-PC1 are similar and give excellent agreement over all energy ranges. At high scattering angles, the calculated values of elastic scattering differential cross-sections overestimate the

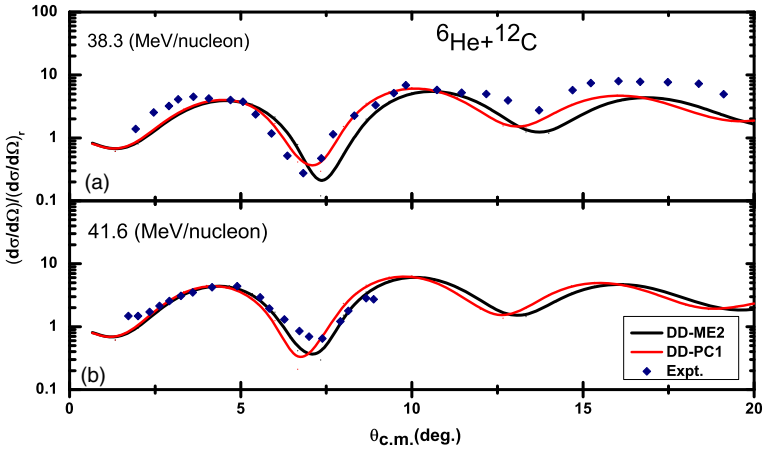

Figure 8. Elastic scattering differential cross-section for ^{6}He projectile on ^{12}C target: (**a**) at an incident energy of 38.3 MeV/nucleon; (**b**) at an incident energy of 41.6 MeV/nucleon. The experimental data are taken from [74,75].

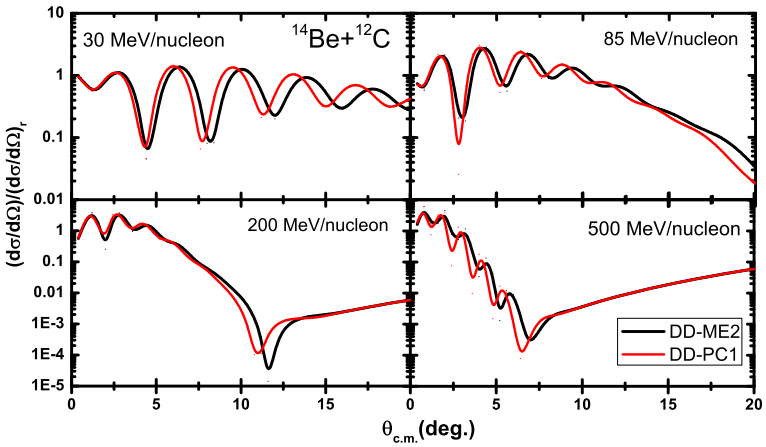

Figure 9. Elastic scattering differential cross-sections for ^{14}Be projectile on ^{12}C target at different energies as a function of scattering angle using the RHB (DD-ME2 and DD-PC1) formalism.

experimental data for ^{12}C+^{12}C system. Figure 7 also shows the comparison of results obtained in the present work with the results using the RMF (NL3) model [41] for ^{12}C+^{12}C system at 30 and 85 MeV/nucleon incident energies. The calculated values in the present work are slightly underestimated whereas the results obtained using RMF (NL3) are slightly overestimated at low angle region. At large angles, both approaches show a similar trend in comparison to the experimental data but fail to have a one-to-one correspondence with experimental results.

Figure 8 shows the differential cross-section for ^{6}He+^{12}C at 38.3 and 41.6 MeV/nucleon incident energies using RHB (DD-ME2 and DD-PC1) densities along with the experimental data [74,75]. From figure 8 we conclude that the RHB densities produce remarkable agreement of differential elastic cross-section with the experimental data. The role of realistic density for the two-neutron halo nucleus ^{6}He is confirmed in ref. [76], where the same experimental data have been analysed using microscopic optical potentials obtained by a double-folding procedure and high-energy approximation. In this approach, the microscopic densities of protons and neutrons in ^{6}He were calculated within the large-scale shell model. In general, it is seen from figure 8 that the experimental data are higher than differential elastic scattering cross-sections for RHB densities at high scattering angles.

Figure 9 presents our calculated values of the differential cross-section for the ^{14}Be+^{12}C system at 30, 85, 200 and 500 MeV/nucleon energies, respectively, using the DD-ME2 and DD-PC1 densities. From figure 9 we can see that the calculated results for RHB (DD-ME2 and DD-PC1) formalism using Glauber model are almost identical and show large variation with incident projectile energy. The DD-ME2 and DD-PC1 calculations produce a small difference up to the first minimum. The

oscillatory structure of the elastic scattering differential cross-section at a low scattering angle increases with the increase of incident projectile energy. It is found that the diffraction pattern decreases with the increase of the scattering angle and disappears at high scattering angles. In the low scattering angle region DD-ME2 and DD-PC1 densities give similar patterns. Overall, this analysis also confirms that the elastic scattering cross-section is well reproduced using the correct wave function together with the profile function used in this study.

4. Conclusions

In summary, we have discussed bulk properties like binding energy and charge radius for light mass nuclei using RHB (DD-ME2 and DD-PC1) formalism. Our theoretical results show a good agreement with the available experimental data. In general, the calculated value of total reaction cross-section σ_r using DD-ME2 densities are better than the result obtained using DD-PC1 densities. We have shown that the calculated values of σ_r are in good agreement with the experimental data. σ_r decreases with the increase of the projectile energy E and σ_r is almost constant at high energy, as observed experimentally too. It has been also found that the total reaction cross-section increases with the increase of the projectile mass. The analysis of the differential scattering cross-section shows a clear diffraction pattern in which the magnitude of separation is large at a small scattering angle and the oscillation keeps on decreasing with an increase in scattering angles, as well as incident energy. It is pertinent to mention that in the present work the nuclear deformation has not been considered explicitly even though it affects the reaction cross-section. Even for large deformation $|\beta_2|\sim 0.2$, it amounts to a variation of about 2% only [51]. Thus, we can conclude that the combined effect of deformation and rotation is significantly smaller than the effect of large neutron excess which is largely embedded in the density profile. Hence, employing reliable density distribution in conjunction with the Glauber model leads to a satisfactory description of the total reaction cross-section and elastic scattering differential cross-section over a wide energy range.

Acknowledgements

Ajeet Singh is highly thankful to the Council of Scientific and Industrial Research, New Delhi for providing Junior Research Fellowship (JRF) under File No. 09/1088(0005)/2018-EMR-1. M K Gaidarov is grateful for the support of the Bulgarian National Science Fund under Contract No. KP-06-N38/1.

References

[1] I Tanihata, *J. Phys. G: Nucl. Part. Phys.* **22**, 157 (1996)
[2] P Arumugam, B K Sharma, P K Sahu, S K Patra, T Sil, M Centelles and X Vinas, *Phys. Lett. B* **601**, 51 (2004)
[3] A Shukla, S Aberg and S K Patra, *J. Phys. G: Nucl. Part. Phys.* **38**, 095103 (2011)
[4] P G Hansen and B Jonson, *Europhys. Lett.* **4**, 409 (1987)
[5] A Ozawa, T Suzuki and I Tanihata, *Nucl. Phys. A* **693**, 32 (2001)
[6] X-X Sun, J Zhao and S-G Zhou, *Phys. Lett. B* **785**, 530 (2018)
[7] A J Miller *et al*, *Nature Phys.* **15**, 432 (2019)
[8] V Morcelle *et al*, *Phys. Rev. C* **89**, 044611 (2014)
[9] I Tanihata *et al*, *Phys. Lett. B* **287**, 307 (1992)
[10] Y Togano *et al*, *Phys. Lett. B* **761**, 412 (2016)
[11] K Tanaka *et al*, *Phys. Rev. Lett.* **104**, 062701 (2010)
[12] W Horiuchi, Y Suzuki, B Abu-Ibrahim and A Kohama, *Phys. Rev. C* **75**, 044607 (2007)
[13] A Ozawa *et al*, *Phys. Rev. Lett.* **84**, 24 (2000)
[14] A N Antonov, M K Gaidarov, D N Kadrev, P E Hodgson and E Moya de Guerra, *Int. J. Mod. Phys. E* **13**, 759 (2004)
[15] A N Antonov, D N Kadrev, M K Gaidarov, E M de Guerra, P Sarriguren, J M Udias, V K Lukyanov, E V Zemlyanaya and G Z Krumova, *Phys. Rev. C* **72**, 044307 (2005)
[16] K Varga, S C Pieper, Y Suzuki and R B Wiringa, *Phys. Rev. C* **66**, 034611 (2002)
[17] B Abu-Ibrahim, Y Ogawa, Y Suzuki and I Tanihata, *Comput. Phys. Commun.* **151**, 369 (2003)
[18] G F Bertsch, H Esbensen and A Sustich, *Phys. Rev. C* **42**, 758 (1990)
[19] K Yabana, Y Ogawa and Y Suzuki, *Phys. Rev. C* **45**, 2909 (1992)
[20] A Bhagwat and Y K Gambhir, *Phys. Rev. C* **69**, 014315 (2004); A Bhagwat, Y K Gambhir and S H Patil, *Eur. Phys. J. A* **8**, 511 (2000)
[21] B. K Sharma, S K Patra, Raj K Gupta, A Shukla, P Arumugam, P D Stevenson and Walter Greiner, *J. Phys. G: Nucl. Part. Phys.* **32**, 2089 (2006)
[22] A Shukla, S Aberg and A Bajpeyi, *J. Phys. G: Nucl. Part. Phys.* **44**, 025104 (2017)
[23] T Niksic, D Vretenar, P Finelli and P Ring, *Phys. Rev. C* **66**, 024306 (2002)
[24] F Hofmann, C M Keil and H Lenske, *Phys. Rev. C* **64**, 034314 (2001)
[25] S Typel and H H Wolter, *Nucl. Phys. A* **656**, 331 (1999)
[26] F de Jong and H Lenske, *Phys. Rev. C* **57**, 3099 (1998)
[27] T Niksic, D Vretenar and P Ring, *Phys. Rev. C* **78**, 034318 (2008)
[28] P Ring, *Prog. Part. Nucl. Phys.* **37**, 193 (1996)
[29] Y Tian, Z Y Ma and P Ring, *Phys. Lett. B* **676**, 44 (2009)
[30] R J Glauber, *Phys. Rev.* **100**, 242 (1955)

[31] R J Glauber, *Lectures in theoretical physics* edited by W E Brittin and L G Dunham (Interscience, New York, 1959), Vol. 1, p. 315
[32] R N Panda, M Panigrahi, Mahesh K Sharma and S K Patra, *Phys. Atom. Nucl.* **81**, 417 (2018)
[33] B Abu-Ibrahim, K Fujimura and Y Suzuki, *Nucl. Phys. A* **657**, 391 (1999)
[34] J Chauvin, D Lubrun, A Lounis and M Buenerd, *Phys. Rev. C* **28**, 1970 (1983)
[35] M Buenerd, A Lounis, J Chauvin, D Lebrun, P Martin, G Duhamel, J C Gondrand and P D Saintignon, *Nucl. Phys. A* **424**, 313 (1984)
[36] P Shukla, *Phys. Rev. C* **67**, 054607 (2003)
[37] A Bhagwat and Y K Gambhir, *Phys. Rev. C* **77**, 027602 (2008); *ibid.* **68**, 044301(2003)
[38] I Sick, *Nucl. Phys. A* **218**, 509 (1974)
[39] X Liu, P Egelhof, O Kiselev and M Mutterer, *Phys. Lett. B* **809**, 135776 (2020)
[40] P J Karol, *Phys. Rev. C* **11**, 1203 (1975)
[41] A Shukla, B K Sharma, R Chandra, P Arumugam and S K Patra, *Phys. Rev. C* **76**, 034601 (2007)
[42] H L Bradt and B Peters, *Phys. Rev.* **77**, 54 (1950)
[43] S Kox *et al*, *Nucl. Phys. A* **420**, 162 (1984)
[44] S Kox *et al*, *Phys. Rev. C* **159**, 15 (1985)
[45] S Kox *et al*, *Phys. Rev. C* **35**, 1678 (1987)
[46] Geant4 Physics Reference Manual
[47] L W Townsend and J W Wilson, *Phys. Rev. C* **37**, 892 (1988)
[48] W Q Shen, B Wang, J Feng, W L Zhan, Y T Zhu and E P Feng, *Nucl. Phys. A* **491**, 130 (1989)
[49] L Sihver, C H Tsao, R Silberberg, T Kanai and A F Barghouty, *Phys. Rev. C* **47**, 1225 (1993)
[50] R K Tripathi, F A Cucinotta and J W Wilson, *Nucl. Instrum. Methods B* **155**, 349 (1999)
[51] K Iida, A Kohama and K Oyamatsu, *J. Phys. Soc. Jpn.* **76**, 044201 (2007)
[52] L Sihver, M Lantz and A Kohama, *Phys. Rev. C* **89**, 067602 (2014)
[53] R K Tripathi, F A Cucinotta and J W Wilson, *Nucl. Instrum. Methods B* **117**, 347 (1996)
[54] H P Wellisch and D Axen, *Phys. Rev. C* **54**, 1329 (1996)
[55] http://www.nndc.bnl.gov/masses/
[56] G Audi, A H Wapstra and C Thibault, *Nucl. Phys. A* **729**, 337 (2003)
[57] S K Patra and C R Praharaj, *Phys. Rev. C* **44**, 2552 (1991)
[58] I Angeli and K P Marinova, *At. Data Nucl. Data Tables* **99**, 69 (2013)
[59] G Hagen *et al*, *Nature Phys.* **12**, 186 (2016)
[60] X Roca-Maza, M Centelles, F Salvat and X Vinas, *Phys. Rev. C* **78**, 044332 (2008)
[61] J Y Hostachy *et al*, *Nucl. Phys. A* **490**, 441 (1988); J Chauvin, D Lebrun, A Lounis and M Buenerd, *Phys. Rev. C* **28**, 1970 (1983)
[62] M Fukuda *et al*, *Phys. Lett. B* **208**, 339 (1991); T Kobayashi *et al*, *Phys Lett. B* **232**, 51 (1989)
[63] M Takachi *et al*, *Nucl. Phys. A* **834**, 412c (2010)
[64] S K Charagi, *Phys. Rev. C* **48**, 452 (1993)
[65] S K Charagi and S K Gupta, *Phys. Rev. C* **41**, 1610 (1990)
[66] S K Charagi and S K Gupta, *Phys. Rev. C* **56**, 1171 (1997)
[67] A Bhagwat and Y K Gambhir, *Phys. Rev. C* **73**, 054601 (2006)
[68] T Zheng *et al, Nucl. Phys. A* **709**, 103 (2002)
[69] T Nagahisa and W Horiuchi, *Phys. Rev. C* **97**, 054614 (2018)
[70] R M De Vries and J C Peng, *Phys. Rev. C* **22**, 1055 (1980)
[71] W Horiuchi, S Hatakeyama, S Ebata and Y Suzuki, *Phys. Rev. C* **93**, 044611 (2016)
[72] A Ingemarsson *et al, Nucl. Phys. A* **653**, 341 (1999)
[73] T Eliyakut-Roshko, R H McCamis, W T H vas Oers, R F Carlson and A J Cox, *Phys. Rev. C* **51**, 1295 (1995)
[74] V Lapoux *et al, Phys. Rev. C* **66**, 034608 (2002)
[75] J S Al-Khalili *et al, Phys. Lett. B* **378**, 45 (1996)
[76] V K Lukyanov, D N Kadrev, E V Zemlyanaya, A N Antonov, K V Lukyanov and M K Gaidarov, *Phys. Rev. C* **82**, 024604 (2010)